



HAL
open science

Ectopic expression of a mechanosensitive channel confers spatiotemporal resolution to ultrasound stimulations of neurons for visual restoration

Sara Cadoni, Charlie Demené, Ignacio Alcalá, Matthieu Provansal, Diep Nguyen, Dasha Nelidova, Guillaume Labernède, Jules Lubetzki, Ruben Goulet, Emma Burban, et al.

► To cite this version:

Sara Cadoni, Charlie Demené, Ignacio Alcalá, Matthieu Provansal, Diep Nguyen, et al.. Ectopic expression of a mechanosensitive channel confers spatiotemporal resolution to ultrasound stimulations of neurons for visual restoration. *Nature Nanotechnology*, 2023, 10.1038/s41565-023-01359-6 . hal-04067358

HAL Id: hal-04067358

<https://hal.sorbonne-universite.fr/hal-04067358v1>

Submitted on 13 Apr 2023

HAL is a multi-disciplinary open access archive for the deposit and dissemination of scientific research documents, whether they are published or not. The documents may come from teaching and research institutions in France or abroad, or from public or private research centers.

L'archive ouverte pluridisciplinaire **HAL**, est destinée au dépôt et à la diffusion de documents scientifiques de niveau recherche, publiés ou non, émanant des établissements d'enseignement et de recherche français ou étrangers, des laboratoires publics ou privés.

1 **Title:**

2

3 **Ectopic expression of a mechanosensitive channel confers spatiotemporal resolution to**
4 **ultrasound stimulations of neurons for visual restoration**

5

6 **Author list:**

7 Sara Cadoni¹, Charlie Demené², Ignacio Alcalá¹, Matthieu Provansal¹, Diep Nguyen¹, Dasha
8 Nelidova³, Guillaume Labernede¹, Jules Lubetzki¹, Ruben Goulet¹, Emma Burban¹, Julie
9 Dégardin¹, Manuel Simonutti¹, Gregory Gauvain¹, Fabrice Arcizet¹, Olivier Marre¹, Deniz
10 Dalkara¹, Botond Roska³, José Alain Sahel^{1,4,5,6}, Mickael Tanter^{2*}, Serge Picaud^{1*}

11

12 **Affiliation:**

13 ¹Sorbonne Université, INSERM, CNRS, Institut de la Vision, 17 rue Moreau, F-75012 Paris,
14 France;

15 ²Physics for Medicine Paris, INSERM, CNRS, École Supérieure de Physique et de Chimie
16 Industrielles (ESPCI Paris), Paris Sciences et Lettes (PSL) Research University, 75012 Paris,
17 France;

18 ³Institute of Molecular and Clinical Ophthalmology Basel, Basel, Switzerland;

19 ⁴Department of Ophthalmology, The University of Pittsburgh School of Medicine, Pittsburgh,
20 PA 15213, United States;

21 ⁵Department of Ophthalmology and Vitreo-Retinal Diseases, Fondation Ophtalmologique
22 Rothschild, F-75019 Paris, France;

23 ⁶Centre Hospitalier National d'Ophtalmologie des XV-XX, F-75012 Paris.

24 *These authors contributed equally to this work.

25

26 Corresponding author: Serge Picaud (serge.picaud@inserm.fr)

27 <http://www.researcherid.com/rid/H-4012-2014>

28

29

30

31

32 **Abstract**

33 Remote and precisely controlled activation of the brain is a fundamental challenge in the
34 development of brain-machine interfaces (BMI) for neurological treatments. Low-frequency
35 ultrasound stimulation can be used to modulate neuronal activity deep in the brain especially
36 after expressing ultrasound-sensitive proteins. But so far, no study has described an
37 ultrasound-mediated activation strategy whose spatiotemporal resolution and acoustic
38 intensity are compatible with the mandatory needs of BMIs, in particular for visual restoration.
39 Here we combined the expression of large-conductance mechanosensitive ion channels
40 (MscL) with uncustomary high-frequency ultrasonic stimulation to activate retinal or cortical
41 neurons over millisecond durations at a spatiotemporal resolution and acoustic energy
42 deposit compatible with vision restoration. The *in vivo* sonogenetic activation of the visual
43 cortex generated a behaviour associated to light perception. Our findings demonstrate that
44 sonogenetics can deliver millisecond pattern presentations via an approach less invasive than
45 current BMIs for visual restoration.

46

47

48

49 **Main text**

50 **Introduction**

51 Brain-machine interfaces (BMIs) based on multi-electrode arrays have met with
52 increasing success in peripheral sensory system rehabilitation strategies, for restoring hearing
53 in the cochlea or sight in the retina^{1, 2}. The restoration of vision is the most demanding
54 challenge for BMIs, as it ultimately requires the 13Hz rate transmission of complex spatial
55 patterns³. Although form perception can be achieved by epicortical or intracortical implants⁴,
56 ⁵, lack of long-term sustainability has intensified the search for non-contact distant activation
57 of neuronal circuits. Optogenetic therapy has provided an alternative, as demonstrated on the
58 retina even at the clinical level⁶. Despite encouraging animal studies⁷⁻⁹, approaches for optical
59 stimulation of the cortex are hindered by the dura mater and by brain scattering and
60 absorption of light requiring invasive light guides¹⁰.

61 Ultrasound (US) waves could potentially overcome these limitations to achieve the non-
62 contact neuromodulation of cortical and subcortical areas of the brains¹¹⁻¹⁷. However, this
63 neuromodulation requires a craniotomy (Fig 1.a) and the use of high US frequencies to
64 reach the required spatial resolution. Switching from 0.5 MHz to 15 MHz would theoretically
65 lead to a 30-fold improvement in resolution (Fig. 1c-e) and a ~27000-fold improvement in
66 neuromodulated volume. Unfortunately, most existing US neuromodulation strategies are
67 restricted to low-frequency¹⁵ or mid-range¹⁸ transmissions resulting in poor spatial resolution
68 (>3 mm) and/or long lasting responses while 30 MHz high frequency was reported to generate
69 inhibitory neuromodulation¹⁹. Other attempts at high-frequency neuromodulation have
70 resulted in high levels of acoustic energy²⁰, with risks of thermal heating²¹ and tissue
71 damage¹⁴.

72 Sonogenetic therapy has proposed to generate a neuronal mechano-sensitivity by
73 ectopic expression of US-sensitive proteins like TRP1 ion channel²², mechanosensitive ion
74 channel of large conductance (MscL)²³, or auditory-sensing protein prestin²⁴ using AAV gene
75 delivery to target specific cell populations^{23, 25, 26} nevertheless without spatiotemporal
76 resolution compatible for vision restoration. A high temporal resolution was shown for MscL
77 only in primary cultured hippocampal neurons with mutations enhancing its pressure
78 sensitivity^{27, 28}, the MscL-G22S mutant boosting US sensitivity of *in vivo* neurons²³.

79

80

81

82 We have here investigated if we can use the MscL channel²⁹ 1) to boost the neuronal
83 sensitivity to US not only *ex vivo* but also *in vivo* , 2) to target a locally defined subset of
84 neurons by gene therapy, 3) to induce responses with a temporal precision (millisecond time
85 delay and recovery) sufficient for visual restoration and 4) to gain more than one order of
86 magnitude in spatial resolution through the *in vivo* use of high-frequency US at low acoustic
87 intensities to prevent adverse effects²⁰.

88

89 **Sonogenetic activation on the *ex vivo* retina**

90 Using the retina as an easily accessible part of the central nervous system, we targeted
91 MscL specifically into rat retinal ganglion cells (RGCs), with *in vivo* intravitreal delivery by an
92 adeno-associated vector (AAV) encoding the *mscL* gene from *Escherichia coli* in its wild-type
93 (WT) form or with the G22S mutation²⁸. An AAV2.7m8³⁰ serotype vector was used to encode
94 MscL fused to the red fluorescent protein tdTomato, under control of the SNCG promoter to
95 target the RGC population³¹. On the eye fundus, tdTomato fluorescence was detected *in vivo*
96 (Fig. 2a). Its expression was restricted to RGCs, as indicated by their double labeling with a
97 specific RGC antibody, RPBMS (Figs 2b, E1b). Expression of the MscL channel seemed to be
98 concentrated at the cell membrane on the soma and axon (Figs 2c, E1) with 24% and 46% of
99 RPBMS-positive cells expressing tdTomato, for the MscL-WT and MscL-G22S proteins,
100 respectively (Fig. 2d).

101 During *ex vivo* recordings of the MscL-expressing retina (Fig. 2e), RGCs displayed strong
102 and sustained ON spiking responses to focused 15 MHz US stimulation (Fig. 2f- left)
103 irrespectively of their ON or OFF responses to light (Fig. E2a). Many RGCs presented responses
104 with very short latencies, 12.2 ± 2.5 ms, (Fig. 2f- left), but some had longer latencies (Fig. 2g).
105 By contrast, non-transfected (NT) retina displayed only long latency responses, 50.4 ± 4.2 ms
106 (Figs 2f-right, 2g). Synaptic blockers (CNQX-LAP4-CPP) abolished US responses in non-
107 transfected retinas but not in MscL-transfected retinas, in which they decreased the number
108 of long latency US responses (LL: latency of more than 45 ms, Fig. 2l, Fig E2c-d). This
109 observation suggests that responses in non-transfected retina originate upstream from RGCs,
110 as previously reported⁴¹. This conclusion was supported by the absence of US response in the
111 retinas of non-transfected blind P23H rats having lost photoreceptors whereas transfected
112 P23H showed a majority of short latency (SL) responses (<45ms) (Fig. 2l, Fig E2c-d). The

113 geometric mean latencies in MscL-tested groups were very different from those for the non-
114 transfected retina especially in the blind p23H retina (Fig. E2c), but the cumulative distribution
115 of latencies further highlighted these differences (Fig. E2d). These results suggested a natural
116 mechanosensitivity in photoreceptors highly reminiscent to that of auditory cells in agreement
117 with the expression of Usher proteins in both sensory cells. These Usher proteins are known
118 for generating the auditory mechanotransduction and likely the phototropism of
119 photoreceptors underlying the Stiles Crawford effect³².

120 MscL expression decreased latency and increased the mean number of cells per retina
121 responding to US (Fig. 2h). Short latency (SL) responding cells expressing MscL were sensitive
122 at much lower US pressures than non-transfected cells and their number increased with
123 increasing US pressures (Fig. 2i). SL US responses also involved higher firing rates and were
124 more sustained than LL US responses (Fig. 2j). Moreover, we observed that the G22S mutation
125 further enhanced the sensitivity of SL RGCs to lower US pressures (Fig. 2k, E1b). We
126 subsequently restricted our analyses to SL US responses (<45ms). Neurons responded to even
127 very short stimulation durations (10 ms), with responses showing a fast return to the control
128 level of activity (Fig. 3a). US response durations were correlated with stimulus duration
129 although a reduction of the firing rate occurred for long stimuli (>100 ms) (Fig. 3c-d). Using
130 different stimulus repetition rates, RGCs were able to follow rhythms up to a 10 Hz frequency
131 (Fig. 3b-e). The Fano factor indicated that the response had a low variability in spike count and
132 possibly high information content (Fig. 3c-e).

133 We then investigated whether different US frequencies (0.5, 2.25 and 15 MHz) affected
134 the spatial resolution of the response, in accordance with the measured US pressure fields
135 (Fig. E3). Transducers were designed with a similar focal distance and numerical aperture, for
136 the transmission of focused beams over different frequency ranges (0.5, 2.25, 15 MHz,
137 corresponding to wavelengths of 3.0, 0.7 and 0.1 mm, respectively) (Fig. 1c-e). Features of the
138 responses evoked by the different US frequencies were found to be similar (Fig. E2e-f)
139 although increasing the frequency from 0.5 MHz (typical of neuromodulation) (Fig. 1c) to 15
140 MHz (Fig. 1e) reduced the focal spot by a factor ~4100 with our transducers. Cells responding
141 to US were widespread over the recorded area for 0.5 and 2.25 MHz, but appeared to be more
142 confined for 15 MHz (Fig. 3f), despite similar acoustic parameters (100ms: 1.1 and 1.3 MPa)
143 for the 2.25 MHz and 15 MHz beams. The acoustic pressure at 0.5 MHz was lower (0.5 MPa)
144 due to electric power limitation of our electronics. The spatial dispersion of activated cells

145 decreased significantly from 1.48 ± 0.12 mm and 1.30 ± 0.18 mm at 0.5 MHz and 2.25 MHz,
146 respectively, to 0.59 ± 0.03 mm at 15 MHz (Fig. 3g). This spatial dispersion was consistent with
147 the size of the measured ultrasound pressure fields (Fig. 1c-e); for the 0.5 MHz transducer, the
148 focal spot was much larger than the MEA chip. The density of activated cells increased
149 significantly with increasing US frequency but on a smaller area (Fig. 3h). US stimulation is
150 more effective at higher frequencies, because lower acoustic power values are required to
151 activate an equivalent number of cells. Indeed, even if the acoustic intensities at 2.25 and 15
152 MHz were quite similar, the acoustic power delivered was almost two orders of magnitude
153 lower at 15 MHz (0.03 W) than at 2.25 MHz (0.82 W). At 15 MHz, moving the focal spot of the
154 US probe above the retina triggered a shift in the area of responding cells (Fig. 3i). The
155 response center was found to move in accordance with the displacement of the US transducer
156 (Fig. 3j). These results demonstrate that our sonogenetic therapy approach can efficiently
157 activate neurons with a millisecond and sub-millimetric precision.

158

159 **Spatiotemporal resolution *in vivo* on the visual cortex**

160 We investigated whether the approach could also be applied to the brain *in vivo*
161 through a cranial window (Fig. 1a,b). As the G22S mutation enhanced the US sensitivity of
162 RGCs *ex vivo*, we expressed MscL-G22S in cortical neurons of the primary visual cortex (V1) in
163 rats. We injected AAV9.7m8 encoding the MscL-G22S channel fused to tdTomato under the
164 control of the neuron-specific CamKII promoter into V1. TdTomato fluorescence was detected
165 in the brain (Fig. 4a) and in cortical slices, particularly in layer 4 (Fig. 4b). Staining with an anti-
166 NeuN antibody showed that 33.4% of cortical neurons in the transfected area expressed
167 tdTomato (Fig. 4c).

168 To measure responses to 15MHz US Stimulations, we placed a micro-EcoG (μ EcoG)
169 electrode array on the cortical surface of V1 (Fig. 4d). In non-transfected (NT) animals, no US-
170 evoked signal was recorded (Fig. 4e-right, $n=3$ rats), whereas, in V1 expressing MscL-G22S, US
171 stimulation of the cortical surface elicited large negative μ EcoG potentials (Fig. 4e-middle, $n=6$
172 rats). These US-evoked negative deflections were different from the recorded visual-evoked
173 potentials (Fig. 4e-left). Amplitudes and durations of the US responses were clearly related to
174 the duration of US stimulations (Fig. 4f, 4h) and US pressures (Fig. 4g). V1 cortical responses
175 were again able to follow a repetition rate of up to 13 Hz (Fig. 4i) even if peak amplitude
176 decreased slightly for increasing stimulation frequencies.

177 The peak depolarization of each channel was measured and linearly interpolated to
178 build pseudocolor activation maps showing sizes of the US-responding cortical area
179 dependent on the US pressure from 0.26 MPa ($0.58 \pm 0.17 \text{ mm}^2$ $n=6$ rats) to 1.27 MPa ($1.41 \pm$
180 0.23 mm^2 $n=5$ rats) (Fig. 4j-l). When the ultrasound probe was moved laterally, the source of
181 the generated neuronal activity moved in a similar direction (Fig. 4k). The spatial location of
182 the evoked potentials moved by 0.29 mm (± 0.09 mm, $n=6$ rats) from the previous location
183 (Fig. 4m, Fig. E5), even though we moved the US transducer in 0.4 mm steps. This discrepancy
184 between the displacement of the activated area and movement of the transducer was
185 certainly related to the 0.3 mm discrete spatial pitch distribution of the electrodes and the
186 lateral spread of activity in the circuit. These results suggest that our approach to sonogenetic
187 therapy could yield a spatial resolution of within 400 μm for stimulations at 15 MHz, the focal
188 spot of our 15 MHz transducer being 276 μm wide (Fig. 1d). This opens up the possibility of
189 targeting small areas (down to 0.58 mm^2 for 0.26 MPa), depending on the pressure level.
190 These very localized US-evoked responses, their dependence on the position of the US probe
191 and their short latencies confirmed that they were due to the activation of MscL-G22S-
192 expressing neurons and not to an indirect response related to auditory activation, as
193 previously suggested by others^{33, 34}.

194 When recording with penetrating electrode arrays (Fig. 4d), V1 neurons expressing
195 MscL-G22S generated sustained responses even to 10 ms-long 15MHz US stimuli (Fig. 5a) with
196 latencies shorter than 10ms (5.10 ± 0.62 ms $n=27$ cells) (Fig. 5b), consistent with a direct US
197 activation. Responding neurons were recorded at various cortical depths, ranging from 100
198 μm to 1 mm (Fig. 5c), the focal spot diameter of the US probe being 3.75 mm in the xz plane.
199 Deep neurons responded reliably to stimuli of decreasing duration, from 50 ms to 10 ms, with
200 similar firing rates, whereas longer stimuli induced responses in a broader population of
201 neurons (Fig. 5d-e). To investigate if an US pattern could be applied for visual restoration at a
202 refreshing rate of up to 13 Hz, we increased progressively the sequence of stimuli. Cortical
203 neurons were able to generate distinct responses to each US stimulus up to a 13 Hz repetition
204 rate (Fig. 5f), but the number of responding cells decreased with increasing stimulus frequency
205 (Fig. 5g). No major tissue temperature increase is expected even at this stimulation rate (Fig.
206 E4).

207

208

209 Behavioral response to the sonogenetic stimulation of the visual cortex

210 To define if US-elicited synchronous activation of MscL-expressing excitatory cortical
211 neurons can induce light perception, we assessed mouse behaviour during an associative
212 learning test including 15 MHz US stimulation of V1 in MscL G22S-transfected ($n=14$) and non-
213 transfected ($n=9$) animals (Fig. 6 and E6). Mice subjected to water deprivation were trained to
214 associate the visible-light stimulation of one eye with a water reward (Fig. 6a)³⁵. This task was
215 learned within four days, as indicated by the increasing success rate during this period, from
216 $30.9 \pm 17.9\%$ (SD) to $86.2 \pm 14.1\%$ (SD) for MscL-G22S-transfected mice (Fig. 6b). The success
217 rate was determined by assessing the occurrence of an anticipatory lick between the light
218 onset and the release of the water reward 500 ms later (Fig. 6a). Only mice reaching a 60%
219 success rate on the 4th day were retained for this analysis and sessions showing a compulsive
220 licking rate were excluded. Following cortical US stimulation on day 5, MscL-G22S-transfected
221 mice achieved a success rate $69.3 \pm 25.4\%$ (SD), the difference of which showed no statistical
222 difference with the success rate following light stimulation on day 4 (Fig. 6b). After a pause
223 during the weekend (day 6-7), the animals retained the task, their success rates showing no
224 statistically significant differences with the one following light stimulation (Fig. 6b). By
225 contrast, in non-transfected animals, the success rate following the US stimulation of their
226 visual cortex dropped to $38.1 \pm 18.5\%$ (SD), the difference with the success rate following light
227 stimulation on the 4th day was highly significant ($p<0.0001$) (Figs 6d, E6). In the AAV-injected
228 mice, we found that the latency of the first anticipatory lick was shorter for sonogenetic
229 stimulation (187.1 ± 37.3 ms; $n=14$, SD) than for stimulation with a light flash (265.9 ± 46.5 ms;
230 $n=23$, SD) (Fig. 6c, E6d). This shorter latency for the US response is consistent with the faster
231 activation of cortical neurons for sonogenetic stimulation than for light stimulation of the eye
232 (Fig. 4e). In transfected mice, success rates increased with pressure (Fig. 6d), suggesting a
233 brighter and/or a larger US-elicited percept with a greater US pressure as described with
234 increasing currents in human patients⁴. Interestingly, the licking frequency during the 500 ms
235 before delivery of the water reward also increased with US pressure (Fig. 6e). These results
236 suggest that the sonogenetic stimulation of the visual cortex generates a perception in mice
237 that is likely associated to a visual perception although more complex visual behaviors as form
238 discrimination would be required for a demonstration.

239

240

241 **Safety issues**

242 Our sonogenetic approach greatly decreased the US pressure required for the
243 activation of RGCs and V1 cortical neurons with stimulation sequences remaining below FDA
244 safety limits (510k, Track 3) for US imaging (e.g. for a 10 ms US stimulus of 0.6 MPa, the non-
245 derated I_{sptp} is 12 W/cm² and the non derated I_{spta} value is 0.12 W/cm²). These very low
246 acoustic pressures and acoustic intensities prevent tissue damage, as they are similar to those
247 that have been widely used in clinical diagnostic imaging for decades³⁶. Moreover, simulations
248 of US-induced heating in brain tissue revealed that typical US parameters (i.e. 20 ms, 1.27
249 MPa) (Fig. 4e-h) increased the local temperature by an estimated 0.12 °C, with even high
250 repetition rates (up to 13 Hz) leading to a moderate temperature increase (<0.3 °C) (Fig. E4c-
251 f). These low-temperature fluctuations (corresponding to “worst-case” scenarios as we used
252 non derated US parameters) and stimulation sequences compliant with FDA limits suggest
253 that our approach had no toxic side effects and that US-elicited responses were not
254 temperature-driven and were therefore probably mediated by mechanical activation of MscL
255 channels by US. The fact that acoustics intensities and pressure used here remained far below
256 the FDA requirements for conventional ultrasonic imaging in clinics
257 (<https://www.fda.gov/media/71100/download>) and generated very low temperature
258 increase in comparison with thermal damaging effects³⁷, raises high hopes for a smooth
259 clinical translation. Moreover, a very recent safety study by Cheng et al¹⁹ demonstrated an
260 absence of brain tissue damages using high frequency activation at ten times higher acoustic
261 intensities (continuous insonication at 11.8 W/cm² compared to our “worst case” I_{spta} 1.56
262 W/cm² for repeated stimulations at 13 Hz rate).

263

264 **Conclusions**

265 The development of remotely controlled cortical and subcortical deep neuronal
266 stimulation techniques is of considerable interest for the treatment of diverse neurological
267 diseases and sensory handicaps. Most previous sonogenetic studies focused on the use of low-
268 frequency US²²⁻²⁴ as in the recent demonstration of MscL-based sonogenetic activation in
269 mouse brain²³. However, such low-frequency US waves lead to limited centimetric spatial
270 resolutions (~5x5x45 mm³) and an uncontrolled spatial beam distribution. An alternative
271 approach to spatially containing US stimulations involves the use of higher US frequencies, but
272 this was thought to demand higher energy levels, exceeding safety limits and favoring tissue

273 damage²⁰. The bacterial MscL channel has been reported to sensitize neurons to US^{23, 27, 28} and
274 to lower the pressure for neuronal activation, but its use for high-spatiotemporal resolution
275 sonogenetic stimulation has yet to be shown to be effective *in vivo*. We here showed that
276 that US activation of MscL-G22S expressed in retinal or cortical neurons resulted in responses
277 with millisecond latencies and a spatial resolution of at least 400 μm in the *xy* plane at a 15
278 MHz frequency. The subsequent neuronal activation throughout the depth of the visual cortex
279 (Fig. 5n-p) led to a behavioral motor response, suggesting light perception by the animal.
280 These sonogenetic responses were genuinely related to MscL expression, as they were not
281 observed in non-transfected animals. Following previous demonstrations that the MscL
282 channel is a suitable sonogenetic actuator^{23, 27, 28}, we provide further evidence that the MscL
283 channel has appropriate kinetics for the activation of neurons at a precise spatiotemporal
284 resolution *in situ* and *in vivo*.

285 The temporal precision of sonogenetics is lower than that achieved with optogenetic
286 (> 40Hz) by the fastest opsins³⁸ and ChrimsonR³⁹, which is successfully restoring vision at the
287 retinal level in patients⁶. MscL only follows a 13 HZ frequency *in vivo*, which is in the same
288 range as the 5-20 Hz achieved *in vivo* by the very sensitive opsin, ChRmine⁴⁰, a frequency range
289 likely sufficient for vision³. The discovery of ChRmine has enabled investigators to stimulate
290 deep into the rodent brain even from above the skull⁴⁰. Future studies will have to examine
291 the spatial resolution of this approach and how it compares to sonogenetics. As for all gene
292 therapies in non-dividing cells, both optogenetic and sonogenetic therapies are expected to
293 be life long lasting as indicated by gene therapy in congenital Leber amaurosis although it did
294 not stop the ongoing degeneration of photoreceptors in patients⁴¹.

295 Restoration of form vision at cortical level was previously achieved with 0.5 to 1 mm
296 surface electrodes spaced more than 1 mm apart⁵ or with 1.5-mm-long penetrating electrodes
297 spaced 400 μm apart⁴. The spatial resolution of the proposed sonogenetic therapy therefore
298 appears to be compatible with the cortical restoration of form vision but with a remote non-
299 contact device. To preserve this spatiotemporal resolution, the ultrasound stimulator will
300 require to be placed directly above the dura mater or above an ultrasound transparent
301 artificial skull⁴². At 15 MHz, the typical penetration depth with negligible heating is typically
302 20 mm. Moreover, the resolution of the approach could be increased by using gene therapy
303 to drive expression in specific cell populations and cell compartments^{31, 43}. Further studies are
304 required to generate an interface for coding visual information into US patterns transmitted

305 by an ultrasonic matrix array onto the visual cortex at a video rate. To reduce the ultrasound
306 load, visual restoration can take advantage of event-based camera, heat-sensitive camera or
307 depth filtering imaging to limit the active pixel number in an image⁴⁴⁻⁴⁶. Therefore, our
308 approach provides great hope for the development of high-resolution visual restoration at the
309 cortical level, through its unique combination of a rapid response, high spatial resolution, and
310 cell selectivity with promoters. Even if this approach requires craniotomy, as for other existing
311 visual prostheses, it provides a less invasive approach based on deep and distant cortical
312 activation from above the dura mater following AAV cortical injections. More generally, it
313 paves the way for a new type of genetic-based brain-machine interface capable of
314 compensating for disabilities and suitable for use in treatments of neurological disorders.

315 **Acknowledgements**

316 The authors would like to thank C. Joffrois, M. Valet, Q. Cesar, M. Desrosiers, S. Fouquet, P.
317 Annic, M. Celik, Z. Raics for technical help and scientific advice. This work was supported by
318 the European Research Council (ERC) Synergy Grant Scheme (holistic evaluation of light and
319 multiwave applications to high-resolution imaging in ophthalmic translational research
320 revisiting the Helmholtzian synergies, ERC Grant Agreement #610110), by the European
321 Union's Horizon 2020 research and innovation programme under grant agreement No.
322 785219 (Graphene Flagship Core 2) No. 881603 (Graphene flagship Core3), by the Foundation
323 Fighting Blindness, La Fondation pour la Recherche Médicale (FRM EQUIPE
324 EQU202106012159), l'UNIM, *la Fédération des Aveugles de France*, Optic 2000, the city of
325 Paris, *Région ile de France*, the *Agence Nationale de la Recherche* (ANR BrainOptoSight), and
326 French state funds managed by the *Agence Nationale de la Recherche* (ANR) within
327 *Programme Investissements d'Avenir, Laboratoire d'Excellence (LABEX) LIFESENSES* (ANR-10-
328 LABX-0065) and *Institut Hospitalo-Universitaire FOReSIGHT* (ANR-18-IAHU-0001), by NIH
329 CORE Grant P30 EY08098 to the Department of Ophthalmology, the Eye and Ear Foundation
330 of Pittsburgh, and from an unrestricted grant from Research to Prevent Blindness, New York,
331 NY.

332

333 **Author Contributions Statement**

334 S.C., C.D. designed the experiments. I.A., M.P. contributed equally. S.C., M.P., G.L., I.A., J.L,

335 R.G., E.B., J.D. carried out the experiments and analyzed the data, M.P., D.N., G.G., F.A., O.M.,
336 D.D., M.S., B.R. provided support for experiments, study design and data analysis, S.P., M.T.,
337 J.S. conceived the idea for this project and supervised the analysis of the data obtained. S.C.,
338 C.D, I.A., M.T., S.P. wrote the manuscript. S.P. and M.T. contributed equally. All authors
339 provided critical feedback on the research and the manuscript.

340

341 **Competing interests Statement**

342 The authors have filed for a patent for devices and methods for sonogenetic stimulation.

343

344 **Tables:** None

345

346 **Figure Legends/Captions**

347 **Fig. 1 Sonogenetics using focused ultrasound beams for visual restoration through the intact dura**
348 **mater: impact of ultrasonic transmission frequency.** (a) Concept of visual restoration with US matrix
349 arrays implanted in a cranial window for localized US neuromodulation of the primary visual cortex in
350 humans. The US beam can be adaptively focused at different locations in the V1 cortex while passing
351 through the intact dura mater, subdural and subarachnoid spaces. (b) Proof-of-concept setup used in
352 this study for V1 sonogenetic activation in rodents, using a high-frequency focused transducer on a
353 craniotomized mouse. (c) Characterization of the radiated field for the 0.5 MHz transducer used in this
354 study. (top) Longitudinal view of the maximal pressure for a monochromatic acoustic field radiated at
355 0.5 MHz by the 25.4 mm \emptyset , 31.75 mm focus transducer. Pressure maximum is reached at 25.9 mm,
356 slightly closer to the transducer than the geometric focal point, which is a documented effect ⁶⁶.
357 (middle) Transverse section of the maximal pressure field at depth $z = 25.9$ mm. (bottom) One-
358 dimensional profile of this transverse section giving the FWHM of the focal spot (4.36 mm at 0.5 MHz).
359 (d) Same characterization for the 2.25 MHz 12.7mm \emptyset 25.4 mm focus transducer. (e) Same
360 characterization for the 15 MHz 12.7mm \emptyset 25.4 mm focus transducer. Note that the maximum
361 pressure is reached very close to the geometric focus (25.21 mm versus 25.4 mm for the geometric
362 focus) for this configuration. The FWHM of the focal spot is 0.276 mm. Figures 1a and 1e were created
363 with Biorender.com.

364

365

366 **Fig. 2 Sonogenetic therapy in rat retinal ganglion cells.** (a) *In vivo* retinal fundus image showing MscL-
367 tdTomato expression. (b-c) Confocal stack projections across the retinal ganglion cell (RGC) layer of a
368 flat-mounted retina. (d) Density of RBPMS-, MscL-positive and double-labeled cells ($n=5$ MscL WT and
369 G22s retinas, *, $p=0.0140$, for RBPMS(+); *, $p=0.0465$, for RBPMS(+)/MscL(+), unpaired two-tailed t
370 test). (e) Schematic diagram of the experimental setup with an image of the retina on MEA electrodes.
371 (f) Representative peristimulus time histograms (PSTHs) for US or visual stimuli in MscL-transfected or
372 non-transfected (NT) RGCs (US stimuli: 15 MHz, 1.27 MPa). (g) RGC response latencies to a 15 MHz US
373 stimulus for MscL ($n=300$ cells, 9 retinas) and NT retinas ($n=41$ cells, 4 retinas). Dotted line: 45 ms
374 latency threshold. (h) Number of cells per retina responding to 15 MHz US stimuli (0.98-1.27 MPa) for
375 MscL ($n=9$ retinas) and NT ($n=4$ retinas) with short (< 45 ms, SL) or long latencies (> 45 ms, LL). *
376 $p=0.0002$, unpaired two-tailed t test. (i) Mean number of SL-responding RGCs per retina following
377 stimulation with US stimuli of increasing pressure for MscL ($n=9$) and NT ($n=4$) retinas. *** $p=0.00008$,
378 *** $p=0.0010$, *** $p=0.0008$, multiple unpaired two-tailed t test. (j) Maximum firing rate and response
379 duration (of SL and LL RGCs from MscL retinas in response to US stimuli of increasing pressure (0.2-
380 1.27 MPa) ($n=9$ retinas, ** $p=0.0017$, * $p=0.0418$, unpaired two-tailed t test). (k) Percentage of SL RGC
381 cells (normalized against the maximum number of responsive cells in each experiment) responding to
382 US stimuli for MscL WT ($n=3$ retinas) and MscL G22S ($n=6$ retinas) retinas. ** $p=0.0065$, ** $p=0.0083$,
383 multiple unpaired two-tailed t test. (l) Ratios of RGCs responding to US stimulation with short (SL) or
384 Long latencies (LL) for MscL and NT retinas ($n=9$ retinas for MscL and 4 for NT), following the application
385 of a cocktail of synaptic blockers (CNQX-CPP-LAP4, $n=3$ retinas for both MscL and NT), and for P23H
386 retinas with and without MscL expression (both $n=3$ retinas). * Conditions with no US-elicited cell
387 responses. Data are presented as mean values +/- SEM. Scale bars represent 100, 20, 200 μ m in b,c,e.

388

389

390

391

392 **Fig. 3 Spatiotemporal properties of sonogenetic retinal responses.** (a-b) Spike density functions (SDFs)
393 of two RGCs from a MscL retina for 15 MHz stimulus durations and repetition frequencies (a: 0.5 Hz
394 repetition rate, b: 10, 20, 50, 200 ms durations). (c) Maximum firing rates for different 15 MHz stimulus
395 durations and mean Fano factor values for all cells (10-20 ms $n=8$ retinas, 50-200 ms $n=9$ retinas). (d)
396 Correlation between response duration and stimulus duration ($n=9$ retinas). (e) Maximum firing rates
397 for different stimulus repetition frequencies and mean Fano factor values for all cells (0.2-2 Hz $n=9$
398 retinas, 5-10 Hz $n=8$ retinas). (f) (Top) Retinas on a MEA chip and corresponding size of the incident US
399 pressure beam (circles represent the FWHM and are centered on the estimated center of response),
400 for 0.5, 2.25 and 15 MHz. (Bottom) Corresponding activation maps representing the normalized firing
401 rates of the cells following US stimulation. Each square box represents an electrode with at least one
402 US-activated cell. (g) Spatial dispersion of activated cells and (h) ratio of the number of activated cells
403 to the stimulated area for the three US frequencies, ****, $p=0.00002$ for panel g, $p=0.00006$ (15 vs
404 2.25 MHz) and $p=0.00005$ (15 vs 0.5 MHz) for panel h, ** $p=0.0008$, * $p=0.0169$, unpaired two-tailed t
405 test. $N=12$ retinas for 0.5 MHz (0.29-0.68 MPa), $n=5$ retinas for 2.25 MHz (1.11-1.62 MPa), $n=9$ retinas
406 for 15 MHz (1.12-1.27 MPa). (i) Heatmaps showing activated cells in a MscL retina following
407 displacements (0.4 and 0.8 mm) of the US transducer. Circles represent the estimated center of the
408 response. (j) Relative displacement of the center of the response following displacement of the 15 MHz
409 US transducer. **** $p=0.00001$, ** $p=0.0018$, unpaired two-tailed t test. $n=9$, 9, and 6 positions for 4,
410 4 and 2 retinas for displacements of 0, 0.4 ± 0.20 and 0.8 ± 0.18 mm (SD), respectively. The dotted gray
411 line represents the theoretical displacement. Data are presented as mean values \pm SEM. Scale bars
412 represent 1 mm in f (top) and 0.5mm in f (bottom) and i.

413

414

415

416 **Fig. 4 Spatial resolution of *in vivo* sonogenetic therapy in V1 cortical neurons.** (a) Image of a rat brain
417 expressing MscL-G22S-tdTomato (red) in V1. (b) Confocal stack projection of a sagittal brain slice
418 expressing MscL G22s-tdTomato (red) and labeled with anti-NeuN antibody (green) and DAPI (blue).
419 The layers of V1 are delineated by dashed white lines. (Lower right) Magnification of layer 4 of V1. (c)
420 Density of NeuN-positive, MscL-positive and double-labeled cells for 3 brain slices. (d) Schematic
421 diagram of the setup used for *in vivo* electrophysiological recordings and US stimulation; (Top right)
422 μ EcoG electrode array placed on V1 of a MscL-transfected rat. (e) (Left) Visual-evoked cortical
423 potentials in response to a 100 ms flash. (Middle) Sonogenetic evoked potentials for 15 MHz US stimuli
424 of various durations. (Right) Absence of US responses on a non-transfected (NT) rat to a 15 MHz
425 stimulus. Black traces represent the mean evoked potential over 100 trials, individually illustrated by
426 the gray traces. The black arrow indicates the stimulus onset. (f) Duration of sonogenetic μ EcoG
427 responses for stimuli of different durations (10 ms $n=58$, 20 ms $n=32$ and 50 ms $n=56$ trials on 6
428 animals). (g) N1 peak amplitude for increasing US pressure, (h) increasing duration and (i) frequency
429 ($n=6$ rats). (j) Pseudocolor activation maps for stimuli of increasing US pressure and (k) for a horizontal
430 displacement of the US transducer by 0.8 mm (the arrow indicates the direction of the displacement).
431 Each black dot represents an electrode of the array. The color bar represents N1 peak amplitude in μ V.
432 (l) Mean activated area for various US pressure values ($n=6$ animals). (m) Relative displacement of the
433 activation center to the previous position following movement of the US transducer by 0.4 mm. $p=1$
434 10^{-12} , one-sample two-tailed t test, $n=37$ positions on 6 animals (Mean: 0.29 ± 0.16 mm, SD). Data are
435 presented as mean values \pm SEM. Scale bars represent 200 and 50 μ m in b, 300 μ m in j-k.

436
437
438

439 **Fig. 5: Temporal resolution of *in vivo* sonogenetic cortical activation.** (a) Spike density functions (SDF)
440 of 58 and 27 neurons recorded with a penetrating multielectrode array in MscL-transfected rats
441 following US stimulation for 50 and 10 ms. (Red: mean trace, grey: individual cells) (b) Response
442 latencies following 50 and 10 ms US stimuli (50 ms $n=58$ cells, mean: 7.5 ± 7.6 ms (SD), 7 rats; 10
443 ms $n=27$ cells, mean: 5.1 ± 3.2 ms (SD), 5 rats). (c) Depth of US-responding cells ($n=58$) in MscL-
444 expressing rats ($n=7$). (d) Instantaneous SDF of responses to US stimuli of different durations (1 Hz
445 stimulus repetition frequency). (e) Maximum firing rates ($n= 27, 22, 58$ cells, SD: 55.8, 56.2, 49.8 ms
446 for 10, 20 and 50 ms stimulation respectively) and numbers of activated neurons upon US stimulations
447 of different durations (US pressure: 1 MPa). (f) Instantaneous SDF of responses to US stimuli of
448 different repetition frequencies (10 ms stimulus duration). (g) Mean maximum firing rate and number
449 of activated neurons upon US stimulation at different stimulus repetition frequencies (10 ms, 1MPa,
450 $n= 27, 40, 30, 10, 13$ cells, SD: 55.8, 50.8, 55.7, 41.5, 58.2 Hz). Data are presented as mean values +/-
451 SEM.

452

453

454

455

456

457

458 **Fig. 6 Behavioural response induced by sonogenetic activation of the V1 cortex in mice following**
459 **associative visual training.** (a) Schematic diagram of the behavioral task performed by mice. Water-
460 restricted animals trained in an associative learning paradigm for light stimulation (LS) with a water
461 reward are subjected to either a light stimulation of the eye (day 1-4) or a US stimulation of V1 at 15
462 MHz (day 5 and 8-10). (b) Mean rates of successful trials for 4 days of training during learning of the
463 association between light stimulation (LS, green, 50 ms) and water reward followed by the US
464 stimulation (US orange, 1.2 MPa) for MscL-G22S transfected mice (between Day 4 LS and Day 5 US: 50
465 ms 1.2 MPa, ns $p=0.0570$. Between Day 5 US and Day 8 US: 50 ms 1.2 MPa, ns $p=0.6079$, two-tailed
466 unpaired t test, Mean: 30.9, 49.9, 77.6, 86.2, 69.3, 62.3, 66.9, 76.5, SD: 17.9, 31.2, 13.9, 14.1, 25.4,
467 35.4, 37.1, 27.7%, $n=14$ animals) (c) Mean time to first lick after light (50 ms) and US stimulation (50
468 ms, 1.2 MPa) (**** $p=0.0000290$, two-tailed unpaired t test, $n=23$ and $n=14$ animals, Mean: 265.9,
469 187.1, SD: 46.5, 37.3 ms for LS and US respectively). (d) Mean rate of successful trials over 4 days of
470 US stimulation for non-transfected (NT) and MscL-G22S transfected mice, following 50 ms of US
471 stimulation at increasing US pressure (ns $p=0.9452$, *** $p=0.0003$, **** $p=0.0000296$, two-tailed
472 unpaired t test, for 0.2, 0.7 and 1.2 MPa, respectively, $n=14$ animals, Mean: 35.2, 60.8, 68.7, SD: 17.5,
473 24.4, 23.6% for MscL-G22S; $n=9$ animals, Mean: 35.7, 27.5, 27.8, SD: 12.4, 11.0, 13.2% for NT). (e)
474 Session anticipatory lick rates for NT and MscL-G22S transfected mice at increasing US pressures (ns
475 $p=0.6934$, * $p=0.0119$, **** $p=0.0000340$, two-tailed unpaired t test, for 0.2, 0.7 and 1.2 MPa,
476 respectively, $n=14$ animals, Mean: 1.4, 3.0, 4.1, SD: 0.4, 1.7, 1.8 Hz for MscL-G22S and $n=9$ animals,
477 Mean: 1.3, 1.4, 1.2, SD: 0.3, 1.1, 0.5 Hz for NT). Data are presented as mean values +/- SEM.

478

479

480 **References**

- 481 1. Lebedev, M.A. & Nicolelis, M.A. Brain-Machine Interfaces: From Basic Science to
482 Neuroprostheses and Neurorehabilitation. *Physiol Rev* **97**, 767-837 (2017).
- 483 2. Lewis, P.M., Ackland, H.M., Lowery, A.J. & Rosenfeld, J.V. Restoration of vision in
484 blind individuals using bionic devices: a review with a focus on cortical visual
485 prostheses. *Brain Res* **1595**, 51-73 (2015).
- 486 3. VanRullen, R. Perceptual Cycles. *Trends Cogn Sci* **20**, 723-735 (2016).
- 487 4. Fernandez, E. et al. Visual percepts evoked with an intracortical 96-channel
488 microelectrode array inserted in human occipital cortex. *J Clin Invest* **131** (2021).
- 489 5. Beauchamp, M.S. et al. Dynamic Stimulation of Visual Cortex Produces Form Vision in
490 Sighted and Blind Humans. *Cell* **181**, 774-783 e775 (2020).
- 491 6. Sahel, J.A. et al. Partial recovery of visual function in a blind patient after optogenetic
492 therapy. *Nat Med* (2021).
- 493 7. Jazayeri, M., Lindbloom-Brown, Z. & Horwitz, G.D. Saccadic eye movements evoked
494 by optogenetic activation of primate V1. *Nat Neurosci* **15**, 1368-1370 (2012).
- 495 8. Ju, N., Jiang, R., Macknik, S.L., Martinez-Conde, S. & Tang, S. Long-term all-optical
496 interrogation of cortical neurons in awake-behaving nonhuman primates. *PLoS Biol*
497 **16**, e2005839 (2018).
- 498 9. Chernov, M.M., Friedman, R.M., Chen, G., Stoner, G.R. & Roe, A.W. Functionally
499 specific optogenetic modulation in primate visual cortex. *Proc Natl Acad Sci U S A*
500 **115**, 10505-10510 (2018).
- 501 10. McAlinden, N. et al. Multisite microLED optrode array for neural interfacing.
502 *Neurophotonics* **6**, 035010 (2019).
- 503 11. Legon, W. et al. Transcranial focused ultrasound modulates the activity of primary
504 somatosensory cortex in humans. *Nat Neurosci* **17**, 322-329 (2014).
- 505 12. Tufail, Y. et al. Transcranial pulsed ultrasound stimulates intact brain circuits. *Neuron*
506 **66**, 681-694 (2010).
- 507 13. Deffieux, T. et al. Low-intensity focused ultrasound modulates monkey visuomotor
508 behavior. *Curr Biol* **23**, 2430-2433 (2013).
- 509 14. Lee, W. et al. Image-Guided Focused Ultrasound-Mediated Regional Brain
510 Stimulation in Sheep. *Ultrasound Med Biol* **42**, 459-470 (2016).
- 511 15. Tufail, Y., Yoshihiro, A., Pati, S., Li, M.M. & Tyler, W.J. Ultrasonic neuromodulation by
512 brain stimulation with transcranial ultrasound. *Nat Protoc* **6**, 1453-1470 (2011).
- 513 16. Legon, W., Bansal, P., Tyshynsky, R., Ai, L. & Mueller, J.K. Transcranial focused
514 ultrasound neuromodulation of the human primary motor cortex. *Sci Rep* **8**, 10007
515 (2018).
- 516 17. Mehic, E. et al. Increased anatomical specificity of neuromodulation via modulated
517 focused ultrasound. *PLoS One* **9**, e86939 (2014).
- 518 18. Kim, S. et al. Transcranial focused ultrasound stimulation with high spatial resolution.
519 *Brain Stimul* **14**, 290-300 (2021).
- 520 19. Cheng, Z. et al. High resolution ultrasonic neural modulation observed via in vivo two-
521 photon calcium imaging. *Brain Stimul* **15**, 190-196 (2022).
- 522 20. Ye, P.P., Brown, J.R. & Pauly, K.B. Frequency Dependence of Ultrasound
523 Neurostimulation in the Mouse Brain. *Ultrasound Med Biol* **42**, 1512-1530 (2016).

- 524 21. Constans, C., Mateo, P., Tanter, M. & Aubry, J.F. Potential impact of thermal effects
525 during ultrasonic neurostimulation: retrospective numerical estimation of
526 temperature elevation in seven rodent setups. *Phys Med Biol* **63**, 025003 (2018).
- 527 22. Yang, Y. et al. Sonogenetics for noninvasive and cellular-level neuromodulation in
528 rodent brain. *bioRxiv* <https://doi.org/10.1101/2020.01.28.919910> (2020).
- 529 23. Qiu, Z. et al. Targeted Neurostimulation in Mouse Brains with Non-invasive
530 Ultrasound. *Cell Rep* **32**, 108033 (2020).
- 531 24. Huang, Y.S. et al. Sonogenetic Modulation of Cellular Activities Using an Engineered
532 Auditory-Sensing Protein. *Nano Lett* **20**, 1089-1100 (2020).
- 533 25. Wu, X. et al. Sono-optogenetics facilitated by a circulation-delivered rechargeable
534 light source for minimally invasive optogenetics. *Proc Natl Acad Sci U S A* (2019).
- 535 26. Yang, Y. et al. Sonothermogenetics for noninvasive and cell-type specific deep brain
536 neuromodulation. *Brain Stimul* **14**, 790-800 (2021).
- 537 27. Ye, J. et al. Ultrasonic Control of Neural Activity through Activation of the
538 Mechanosensitive Channel Mscl. *Nano Lett* **18**, 4148-4155 (2018).
- 539 28. Soloperto, A. et al. Mechano-sensitization of mammalian neuronal networks through
540 expression of the bacterial large-conductance mechanosensitive ion channel. *J Cell*
541 *Sci* **131** (2018).
- 542 29. Sukharev, S.I., Blount, P., Martinac, B., Blattner, F.R. & Kung, C. A large-conductance
543 mechanosensitive channel in *E. coli* encoded by mscl alone. *Nature* **368**, 265-268
544 (1994).
- 545 30. Dalkara, D. et al. In vivo-directed evolution of a new adeno-associated virus for
546 therapeutic outer retinal gene delivery from the vitreous. *Sci Transl Med* **5**, 189ra176
547 (2013).
- 548 31. Chaffiol, A. et al. A New Promoter Allows Optogenetic Vision Restoration with
549 Enhanced Sensitivity in Macaque Retina. *Mol Ther* **25**, 2546-2560 (2017).
- 550 32. Verschueren, A. et al. Planar polarity in primate cone photoreceptors: a potential role
551 in Stiles Crawford effect phototropism. *Commun Biol* **5**, 89 (2022).
- 552 33. Sato, T., Shapiro, M.G. & Tsao, D.Y. Ultrasonic Neuromodulation Causes Widespread
553 Cortical Activation via an Indirect Auditory Mechanism. *Neuron* **98**, 1031-1041 e1035
554 (2018).
- 555 34. Guo, H. et al. Ultrasound Produces Extensive Brain Activation via a Cochlear Pathway.
556 *Neuron* **98**, 1020-1030 e1024 (2018).
- 557 35. Nelidova, D. et al. Restoring light sensitivity using tunable near-infrared sensors.
558 *Science* **368**, 1108-1113 (2020).
- 559 36. ter Haar, G. Ultrasound bioeffects and safety. *Proc Inst Mech Eng H* **224**, 363-373
560 (2010).
- 561 37. Sapareto, S.A. & Dewey, W.C. Thermal dose determination in cancer therapy. *Int J*
562 *Radiat Oncol Biol Phys* **10**, 787-800 (1984).
- 563 38. Aravanis, A.M. et al. An optical neural interface: in vivo control of rodent motor
564 cortex with integrated fiberoptic and optogenetic technology. *J Neural Eng* **4**, S143-
565 156 (2007).
- 566 39. Klapoetke, N.C. et al. Independent optical excitation of distinct neural populations.
567 *Nat Methods* **11**, 338-346 (2014).
- 568 40. Chen, R. et al. Deep brain optogenetics without intracranial surgery. *Nat Biotechnol*
569 **39**, 161-164 (2021).

- 570 41. Daich Varela, M., Cabral de Guimaraes, T.A., Georgiou, M. & Michaelides, M. Leber
571 congenital amaurosis/early-onset severe retinal dystrophy: current management and
572 clinical trials. *Br J Ophthalmol* **106**, 445-451 (2022).
- 573 42. Flores, A.R. et al. Safety, Feasibility, and Patient-Rated Outcome of Sonolucent
574 Cranioplasty in Extracranial-Intracranial Bypass Surgery to Allow for Transcranioplasty
575 Ultrasound Assessment. *World Neurosurg* **144**, e277-e284 (2020).
- 576 43. Greenberg, K.P., Pham, A. & Werblin, F.S. Differential targeting of optical
577 neuromodulators to ganglion cell soma and dendrites allows dynamic control of
578 center-surround antagonism. *Neuron* **69**, 713-720 (2011).
- 579 44. Lorach, H. et al. Artificial retina : The multichannel processing of the mammalian
580 retina achieved with a neuromorphic asynchronous light acquisition device. *J Neural*
581 *Eng* **9**, 066004 (2012).
- 582 45. Kartha, A. et al. Prosthetic Visual Performance Using a Disparity-Based Distance-
583 Filtering System. *Transl Vis Sci Technol* **9**, 27 (2020).
- 584 46. Montezuma, S.R. et al. Improved localisation and discrimination of heat emitting
585 household objects with the artificial vision therapy system by integration with
586 thermal sensor. *Br J Ophthalmol* **104**, 1730-1734 (2020).
- 587
- 588

589 **Methods**

590 **Animals**

591 Experiments were conducted in accordance with the National Institutes of Health Guide for
592 the Care and Use of Laboratory Animals. Protocols were approved by the Local Animal Ethics
593 Committee (Committee Charles Darwin no. 5, registration number 9529 and 26889) and
594 conducted in agreement with Directive 2010/63/EU of the European Parliament. Long Evans
595 male rats aged between 2 and 12 months and wild-type male mice (C57BL/6J) aged 9 weeks
596 were obtained from Janvier Laboratories, P23H (line 1) male transgenic rats (9-22 months)
597 were raised locally.

598

599 **Plasmid cloning & AAV production**

600 Plasmids containing the *Escherichia coli* *mscL* sequence in the WT form and with the G22S
601 mutation were obtained from Francesco Difato (Addgene plasmids #107454 and #107455)²⁸.
602 To target retinal ganglion cells, the SNCG promoter³¹ was inserted into an AAV backbone
603 plasmid containing the *mscL* sequence fused to the tdTomato gene and the Kir2.1 ER export
604 signal, to drive expression at the plasma membrane. An AAV2.7m8 vector was used for intra-
605 vitreous delivery. For targeting neurons in V1 cortical layers, the SNCG promoter was replaced
606 by the CamKII promoter and an AAV9.7m8 vector was chosen. Recombinant AAVs were
607 produced by the plasmid cotransfection method, and the resulting lysates were purified by
608 iodixanol purification³¹.

609

610 **US stimulus**

611 Three focused ultrasound transducers with different central frequencies were used: 0.5 MHz
612 (diameter $\varnothing = 1$ inch = 25.4mm, focal distance $f = 1.25$ inch = 31.7 mm) (V301-SU, Olympus),
613 2.25 MHz ($\varnothing = 0.5$ inch = 12.7 mm, $f = 1$ inch = 25.4 mm) (V306-SU, Olympus) and 15 MHz (\varnothing
614 = 0.5 inch = 12.7 mm, $f = 1$ inch = 25.4 mm) (V319-SU, Olympus), corresponding to numerical
615 apertures $F/\varnothing = 1,25$ and 2. Acoustic fields radiated by those three focused transducers are
616 presented in Figure 1 (simulations) and extended figure E3 (experimental measurements). A
617 TiePie Handyscope (HS5, TiePie Engineering) was used to produce the stimulus waveform,
618 which was then passed through an 80 dB RF power amplifier (VBA 230-80, Vectawave)
619 connected to the transducer. Transducer pressure outputs (pressure at focus, 3D pressure

620 maps) were measured in a degassed water tank with a Royer-Dieulesaint heterodyne
621 interferometer⁴⁷. US stimuli used for *ex vivo* and *in vivo* stimulation had the following
622 characteristics: 1 kHz pulse repetition frequency with a 50% duty cycle, sonication duration
623 between 10 and 200 ms and inter-stimulus interval between 0.01 and 2 s. Peak acoustic
624 pressures were ranging from 0.11-0.88 MPa, 0.3-1.6 MPa, 0.2-1.27 MPa, for the 0.5, 2.25 and
625 15 MHz transducers, respectively. The corresponding estimated Isppa values were 0.39-25.14
626 W/cm², 2.92-83.12 W/cm² and 1.30-52.37 W/cm².

627

628 **Intra-vitreous gene delivery and retinal imaging**

629 Rats were anesthetized⁴⁸ and AAV suspension (2 μ l), containing between 8 and 14 x 10¹⁰ viral
630 particles, was injected into the center of the vitreous cavity. One month later, tdTomato
631 fluorescence imaging was performed on the injected eyes, with a Micron IV retinal imaging
632 microscope (Phoenix Research Laboratories) and Micron Discover V2.2.

633

634 **MEA recordings**

635 Retinal pieces were flattened on a filter membrane (Whatman, GE Healthcare Life Sciences)
636 and placed on a poly-L-lysine (0.1%, Sigma) coated multi-electrode array (electrode diameter
637 30 μ m, spacing 200 μ m, MEA256 200/30 iR-ITO, MultiChannel Systems) with RGCs facing the
638 electrodes³¹. AMPA/kainate glutamate receptor antagonist 6-cyano-7-nitroquinoxaline-2,3-
639 dione (CNQX, 25 μ M, Sigma-Aldrich), the NMDA glutamate receptor antagonist [3H]3-(2-
640 carboxypiperazin-4-yl) propyl-1-phosphonic acid (CPP, 10 μ M, Sigma- Aldrich) and a selective
641 group III metabotropic glutamate receptor agonist, L-(+)-2-amino-4-phosphonobutyric acid (L-
642 AP4, 50 μ M, Tocris Bioscience), were bath-applied through the perfusion line. Light stimuli
643 were delivered with a digital micro-mirror display (DMD, Vialux, resolution 1024x768) coupled
644 to a white LED light source (MNWHL4, Thorlabs) focused on the photoreceptor plane
645 (irradiance 1 μ W/cm²). US transducers were coupled with a custom-made coupling cone filled
646 with degassed water, mounted on a motorized stage (PT3/M-Z8, Thorlabs) placed
647 orthogonally above the retina. The reflected signal of the MEA chip and the retina was
648 detected with an US-key device (Lecoeur Electronique). The distance between the retina and
649 the transducer was equal to the focal length of the transducer; this was verified with the flight
650 time of the reflected signal. From RGC recordings with a 252-channel preamplifier and
651 MC_Rack V4.6.2 (MultiChannel Systems), spikes were sorted with SpykingCircus 0.5

652 software⁴⁹. RGC responses were analyzed with custom scripts written in Matlab (MathWorks
653 2018b) for classification as ON, ON-OFF or OFF, with the response dominance index⁵⁰.
654 Latencies were calculated as the time between stimulus onset and the maximum of the
655 derivative of spike density function. Two classes of US-responding cells were identified on the
656 basis of latency — short and long latency — by fixing a threshold equal to the minimum of the
657 latency distribution of the responses of non-transfected cells to US (45 ms). We determined
658 the peak value A of spike density function for the calculation of response duration, which was
659 defined as the time interval between the two time points for which the SDF was equal to A/e
660 (e : Euler's number). The Fano factor, quantifying spike-count variability, was calculated as
661 the ratio of the variance of the spike-count to the mean. The Euclidean distance between two
662 activated cells was weighted according to the maximum firing rate of the cells. The ratio of
663 the number of activated cells to the size of the area stimulated on the MEA chip was calculated
664 considering the size of the US focal spot for 2.25 and 15 MHz and the size of the MEA for 0.5
665 MHz, because the focal spot was larger than the MEA for this frequency. The center of the
666 response was estimated by weighting the maximum firing rate of each cell by its distance from
667 other responding cells, and the displacement of the response was calculated as the Euclidean
668 distance between two center-of-response positions.

669

670 **Intracranial injections**

671 AAV suspensions were injected into the right hemisphere at two different locations in rats (2.6
672 mm ML, 6.8 mm AP and 3.1 mm ML, 7.2 mm AP from bregma) or at one location in mice (2.5
673 mm ML, 3.5 mm AP from bregma)⁴⁸. For rat injection, the suspension (200 nl, containing 0.2 -
674 8×10^{15} viral particles) was injected at three different depths (1100, 1350 and 1500 μm DV)
675 with a micro-syringe pump controller (Micro4, World Precision Instruments) operating at a
676 rate of 50 nl/min and a 10 μl Hamilton syringe. In mice, AAV suspension (1 μl containing 0.2 -
677 8×10^{15} viral particles) was injected at -400 μm DV at a rate of 100 nL/min.

678

679 ***In vivo* extracellular recordings**

680 One month after AAV injections, a small craniotomy (5x5 mm square) was drilled above V1 in
681 the right hemisphere⁴⁸. TdTomato fluorescence was checked with a Micron IV retinal imaging
682 microscope and Micron Discoverer V2.2 (Phoenix Research Laboratories). A 32-site μEcog
683 electrode array (30 μm electrode diameter, 300 μm electrode spacing, FlexMEA36,

684 MultiChannel Systems) was positioned over the transfected region or in a similar zone for
685 control rats. Multi-electrode (MEA) recordings were performed with a 16-site silicon
686 microprobe tilted at 45° to the brain surface (electrode diameter 30 μm, spacing 50 μm,
687 A1x16-5mm-50-703, NeuroNexus Technologies) and MC_Rack V4.6.2. The MEA was advanced
688 1100 μm into the cortex with a three-axis micromanipulator (Sutter Instruments, Novato, CA).
689 US transducers were coupled to the brain with a custom-made coupling cone filled with
690 degassed water and US gel on a motorized stage. The distance between the cortex and the
691 transducer was equal to the focal length of the transducer. Visual stimuli were generated by
692 a white light-collimated LED (MNWHL4, Thorlabs) placed 15 cm away from the eye (4.5
693 mW/cm² at the cornea). Recordings were digitized with 32- and 16-channel amplifiers (model
694 ME32/16-FAI-μPA, MultiChannel Systems). μEcog recordings were analyzed with custom-
695 developed Matlab scripts, MEA recordings with SpykingCircus software and custom-
696 developed Matlab scripts. Response duration was calculated as the interval between the two
697 time points at which the cortical evoked potential was equal to A/e (where A is peak
698 depolarization and e is Euler's number). The activated area was defined as the area of the
699 pseudocolor activation map over which peak depolarization exceeded the background noise
700 level calculated as 2 times the standard deviation of the signal. The response center was
701 estimated by weighting the peak depolarization of each electrode by its distance from other
702 electrodes. Its relative displacement when moving the US transducer, was calculated as the
703 Euclidean distance of the two positions. For intracortical recordings, cell latency was
704 estimated as the time between stimulus onset and the maximum of the derivative of spike
705 density function.

706

707 **Surgery for *in vivo* behavioral testing**

708 C57BL6J mice were injected subcutaneously with Buprenorphine (0,05 mg/kg) (Buprécare,
709 Axience), and Dexamethasone (0,7 mg/kg) (Dexazone, Virbac). Animals were anesthetized
710 with Isoflurane (5% induction, 2% maintenance, in air/oxygen mixture) and the head was
711 shaved and cleaned with antiseptic solution. Animals were head-fixed on a stereotactic frame
712 with an Isoflurane delivering system, eye ointment and a black tissue were applied over the
713 eyes. Body temperature was maintained at 37°C. After a local injection of Lidocaine (4 mg/kg)
714 (Laocaine, Centravet), an incision of the skin was made. Two screws were fixed in the skull,
715 after a small craniotomy (approximately 5 mm x 5 mm) was drilled above V1 in the right

716 hemisphere (0.5 mm steel drill) and cortex buffer was applied. The cortex was covered with a
717 TPX plastic sheet (125 μm thick) and sealed with dental acrylic cement (Tetric Evoflow). For
718 behavioral experiments, a metallic headbar (Phenosys) for head fixation was then glued to the
719 skull on the left hemisphere with dental cement (FUJUCEM II). Animals were placed in a
720 recovery chamber, with subcutaneous injection of physiological serum and ointment on the
721 eyes (Ophtalon, Centravet). Buprenorphine was injected during post-surgery monitoring.

722

723 **Mouse behavioral tests**

724 Mice were placed on a water restriction schedule until they reached approximately 80-85% of
725 their weight. Following habituation to the test conditions³⁵, mice were trained to respond to a
726 light stimulus by performing a voluntary detection task: licking a waterspout (blunt 18G
727 needle, approximately 5 mm from mouth) in response to white light full-field stimulation (200
728 and 50 ms long) of the left eye (dilated with tropicamide, Mydriaticum Dispersa) 35 trials per
729 stimulation duration so 70 trials per day. Water ($\sim 4 \mu\text{L}$) was automatically dispensed 500 ms
730 after the light was switched on, through a calibrated water system. The behavioral protocol
731 and lick detection were controlled by a custom-made system³⁵. The next four days (two-day
732 break during the weekend), US stimulations were delivered on V1 for 50 ms at three different
733 pressure values (0.2, 0.7 and 1.2 MPa). These pressure values were delivered in a different
734 order each day (35 trials each). Inter-trial intervals varied randomly and ranged between 10
735 and 30 s. The 15 MHz US transducer was coupled to the brain with a custom-made coupling
736 cone filled with water and US gel. The success rate was calculated by counting the number of
737 trials in which mice performed anticipatory licks (between stimulus onset and the opening of
738 the water valve). The session anticipatory lick rate shown in Fig. 6e was calculated by
739 subtraction from the anticipatory lick rate of a trial, the spontaneous lick rate (calculated on
740 all the 1 s time windows before each individual stimulus onset (see figure 6a) for all trials) and
741 multiplication by the success rate. Lick latency was calculated by determining the time to the
742 first anticipatory lick after stimulus onset. Mice retained for analysis presented a success rate
743 superior or equal to 60% on the 4th day following light stimulation (LS). Then, Light or US
744 sessions showing a compulsive licking behaviour were excluded based on the outlier
745 identification made using ROUT method (Q = 1%) on the session spontaneous lick rate
746 averaging the measurements on all the trials of the session in the 1s time window before the
747 stimulus onset of the trial.

748

749 **Immunohistochemistry and confocal imaging**

750 Samples were incubated overnight at 4 °C with a monoclonal anti-RBPMS antibody (1:500,
751 Rabbit, ABN1362, Merck Millipore) for the retina³¹, with a monoclonal anti-NeuN antibody
752 (1:500; Mouse, clone A60, MAB377, Merck Millipore) for brain sections⁴⁸. The sections were
753 then incubated with secondary antibodies conjugated with Alexa Fluor 488 (1:500; Donkey
754 anti-Mouse and Donkey anti-Rabbit IgG 488, polyclonal, A-21202 and A-21206, Invitrogen) and
755 DAPI (1:1000, D9542, Merck Millipore) for 1 h at room temperature. An Olympus FV1000
756 confocal microscope with 20x objective (UPLSAPO 20XO, NA: 0.85) was used to acquire images
757 of flat-mounted retinas and brain sections (Software FV10-ASW V04.02).

758 On confocal images processed with FIJI (ImageJ 1.53q), RBPMS- and NeuN-positive cells were
759 counted automatically with the *Analyze particles* FIJI plugin. Cells were counted manually by
760 two different users, with the CellCounter FIJI plugin. Quantification was performed by
761 acquiring confocal stacks in at least four randomly chosen transfected regions of 0.4 mm² (Fig.
762 E1). For V1 neurons, the sagittal brain slice with the largest tdTomato fluorescence zone was
763 selected for each animal. A ROI in V1 was manually defined and quantifications were
764 performed in at least six randomly chosen regions of 0.4 mm².

765

766 **US-induced tissue-heating simulations**

767 A three-fold process was used for the estimation of thermal effects: 1) simulation of the
768 acoustic fields generated by the three transducers, with realistic acoustic parameters, 2)
769 verification that non-linear acoustics did not play an important role in heat transfer and 3)
770 realistic simulations of heat transfer and temperature rise induced at the focus by US in a
771 linear regime for parameters used in this study.

772 For non-linear simulations, we used Matlab's toolbox *kWave*, by defining the geometry of the
773 transducer in 3D, and using the following parameters for the propagation medium (water):
774 sound speed $c = 1500 \text{ m s}^{-1}$, volumetric mass $\rho = 1000 \text{ kg m}^{-3}$, non-linearity coefficient $B/A =$
775 5 , attenuation coefficient $\alpha = 2.2 \cdot 10^{-3} \text{ dB cm}^{-1} \text{ MHz}^{-\gamma}$, and frequency power law of the
776 attenuation coefficient $\gamma = 2$ ⁵¹. We simulated quasi-monochromatic 3D wave-fields using long
777 bursts of 50 cycles; this gave us both the maximum pressure field in 3D and the waveform at
778 the focus. Simulations were calibrated by adjusting the input pressure (excitation of the
779 simulated transducer) to reach the pressure at the focus measured in the water tank with the

780 real transducers. The FWHM focal spot diameter in the xy plane was 4.36, 1.61 and 0.276 mm,
781 and the major axis in the xz plane was 32.3, 20.6 and 3.75 mm long for the 0.5, 2.25 and 15
782 MHz transducers, respectively (Fig. 1b-d). Non-linear effects were evaluated by estimating the
783 relative harmonic content of the waveform at the focus. In the 15 MHz focus transducer
784 example in figure 1d, the experimental and simulated signals at the focal spot were compared
785 and found to be highly concordant (Fig. E4a). Furthermore, the amplitude of the second
786 harmonic is 19.8 dB below the fundamental (20.9 dB in the simulated case), meaning that if
787 the fundamental energy is E, the second harmonic has energy E/95 (Fig. E4b). Therefore, we
788 can reasonably neglect the non-linear effects in the calculations of the thermal effects, as they
789 account for ~1% of the energy involved. The same conclusions were drawn at 0.5 MHz and 15
790 MHz. Linear wave propagation approximations considerably decreased the computing cost of
791 the simulations. Linear propagation simulations were conducted with the *Field II* toolbox in
792 Matlab^{52, 53}, in monochromatic mode, with the same medium properties as *kWave* (water), to
793 obtain the 3D maximum pressure fields. These maximum pressure fields were used to build a
794 heating source term $Q_{US} = \frac{\alpha_{np} p_{max}^2}{\rho_b c_b}$, where α_{np} is the absorption coefficient of the brain at
795 the considered frequency (59.04 Np m⁻¹ at 15 MHz, calculated from $\alpha_{brain} = 0.21 \text{ dB cm}^{-1} \text{ MHz}^{-\nu}$
796 and $\nu = 1.18$), the brain volumetric mass $\rho_{brain} = 1046 \text{ kg m}^{-3}$, the brain sound speed $c_{brain} =$
797 1546 m s^{-1} ^{61,64}, and p_{max} is the 3D maximum pressure field. This source term was then used
798 in the resolution of a Pennes's bioheat equation $\rho_{brain} C_{brain} \cdot \frac{\partial T}{\partial t} = \text{div}(K_t \cdot \nabla T) -$
799 $\rho_{blood} C_{blood} P_{blood} (T - T_a) + Q$ in *kWave*, where C_{brain} is the blood specific heat capacity
800 (3630 J.kg⁻¹ °C⁻¹), K_t the brain thermal conductivity (0.51 W.m⁻¹ °C⁻¹), ρ_{blood} the blood density
801 1050 kg m⁻³, C_{blood} the blood specific heat capacity (3617 J.kg⁻¹ °C⁻¹), P_{blood} the blood
802 perfusion coefficient (9.7 10⁻³ s⁻¹), T_a the arterial temperature (37°C), and $Q = Q_{US} +$
803 $\rho_{brain} \cdot \gamma_{brain}$ with γ_{brain} the heat generation of the brain tissue (11.37 W kg⁻¹)^{54, 55}. The initial
804 condition for brain temperature was set to $T_0 = 37 \text{ °C}$.

805

806 This simulation corresponds to the worst-case scenario regarding the temperature rise given:
807 1) that the acoustic propagation is simulated in water only (non derated value), with a lower
808 attenuation coefficient (2.2 10⁻³ dB cm MHz⁻²) than the brain (0.59 dB cm MHz^{-1.27}), even if a
809 part of the propagation occurs within the brain. p_{max} maps are, therefore, overestimated. 2)
810 thermal absorption is simulated in brain tissue only, with a higher absorption coefficient (0.21

811 dB cm MHz^{-1.18}) than water, even if a part of the maximum pressure field is actually located
812 within the water of the acoustic coupling cone. Q_{US} is, therefore, slightly overestimated. We
813 mapped the temperature in three spatial dimensions and time, and looked for the point of
814 maximal temperature rise (Fig. E4 c-f).

815

816 **Statistical analysis**

817 Statistical analyses were carried out with Prism software (Prism 9, GraphPad). Values are
818 expressed and represented as means \pm the standard error of the mean (SEM) on figures and
819 in the text unless specified. Data were analyzed in unpaired Welch's *t*-tests (two-tailed) or an
820 unpaired multiple *t*-tests with Sidak- Bonferroni correction for multiple comparisons.
821 Statistical tests are provided in figure legends.

822

823 **Data availability**

824 Data supporting the findings of this study are available within the paper and Supplementary
825 information as well as on FigShare :

826 [https://figshare.com/projects/Ectopic_expression_of_a_mechanosensitive_channel_confers](https://figshare.com/projects/Ectopic_expression_of_a_mechanosensitive_channel_confers_spatiotemporal_resolution_to_ultrasound_stimulations_of_neuronal_circuits_for_visual_restitution/154041)
827 [_spatiotemporal_resolution_to_ultrasound_stimulations_of_neuronal_circuits_for_visual_r](https://figshare.com/projects/Ectopic_expression_of_a_mechanosensitive_channel_confers_spatiotemporal_resolution_to_ultrasound_stimulations_of_neuronal_circuits_for_visual_restitution/154041)
828 [estoration/154041](https://figshare.com/projects/Ectopic_expression_of_a_mechanosensitive_channel_confers_spatiotemporal_resolution_to_ultrasound_stimulations_of_neuronal_circuits_for_visual_restitution/154041).

829 All other data are available from the corresponding author upon reasonable request.

830

831 **Code availability**

832 The custom Matlab codes are available from the corresponding author upon request.

833

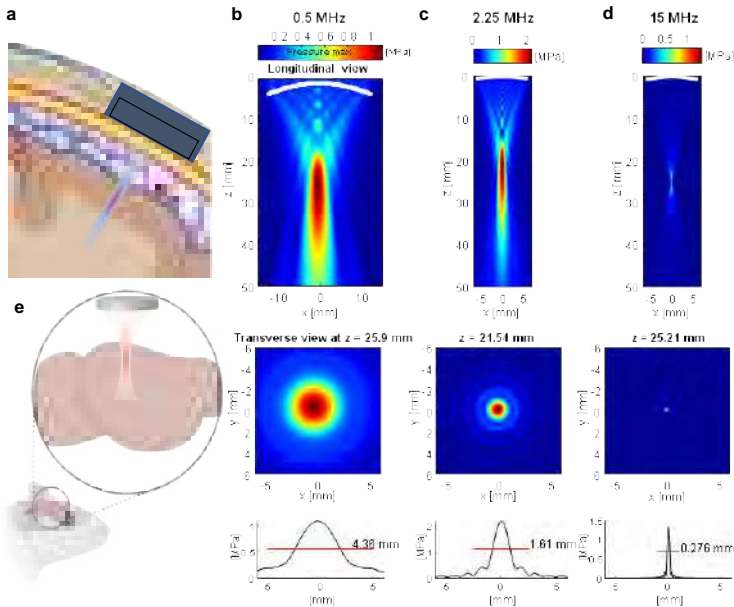
834 **Methods-only references**

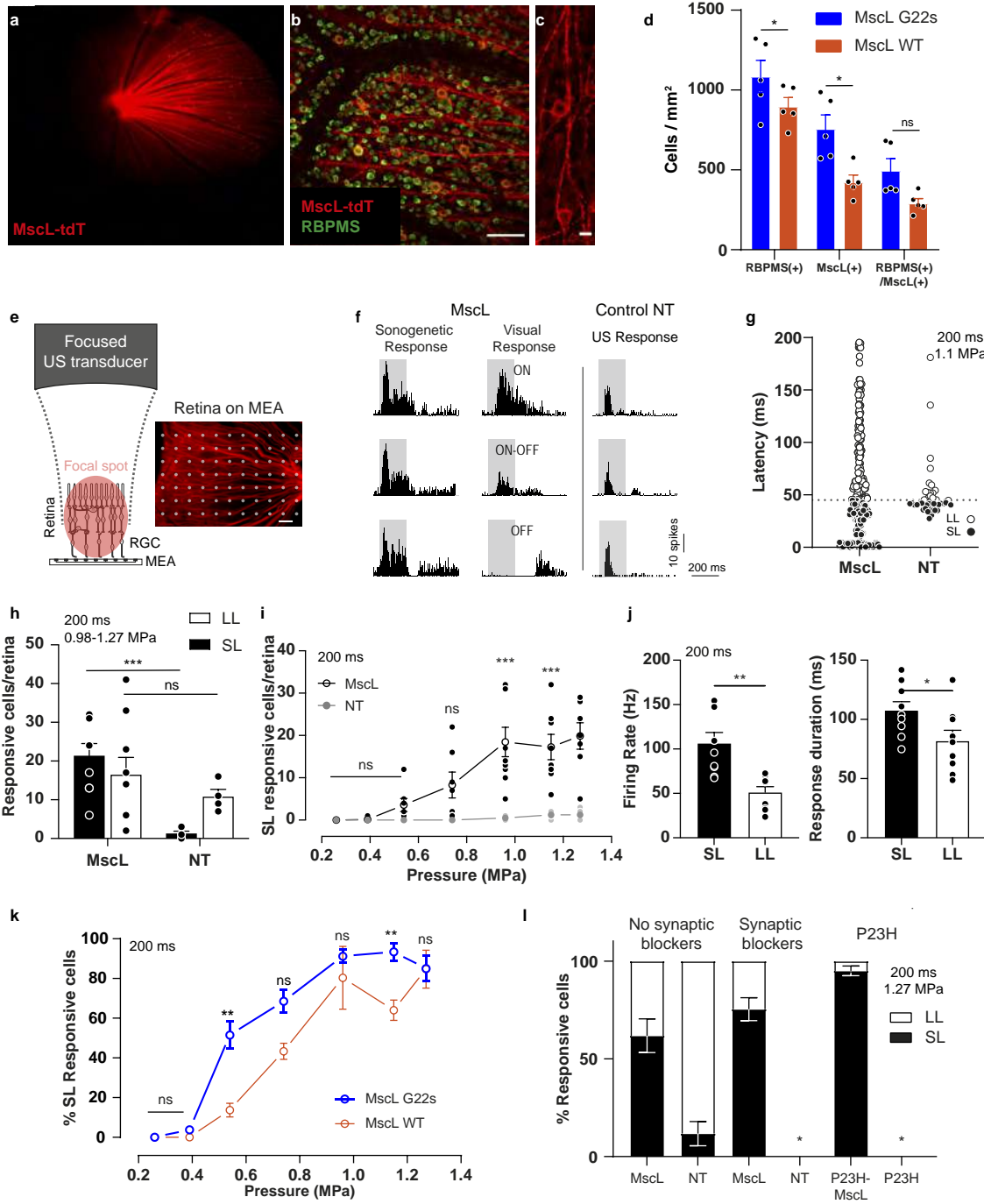
- 835 47. Royer, D. & Dieulesaint, E. Optical probing of the mechanical impulse response of a
836 transducer. . *Applied Physics Letters* **49**, 1056–1058 (1986).
- 837 48. Provansal, M. et al. Functional ultrasound imaging of the spreading activity following
838 optogenetic stimulation of the rat visual cortex. *Sci Rep* **11**, 12603 (2021).
- 839 49. Yger, P. et al. A spike sorting toolbox for up to thousands of electrodes validated with
840 ground truth recordings in vitro and in vivo. *Elife* **7** (2018).
- 841 50. Akerman, C.J., Smyth, D. & Thompson, I.D. Visual experience before eye-opening and
842 the development of the retinogeniculate pathway. *Neuron* **36**, 869-879 (2002).
- 843 51. Duck, F.A. A. Physical Properties of Tissues: A Comprehensive Reference Network. ,
844 (Academic Press,). *Ultrasound in Medicine & Biology* **36**, (Academic Press) (1990).

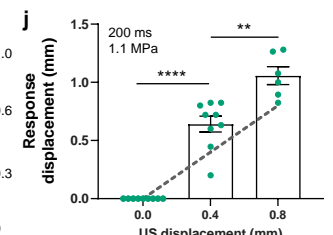
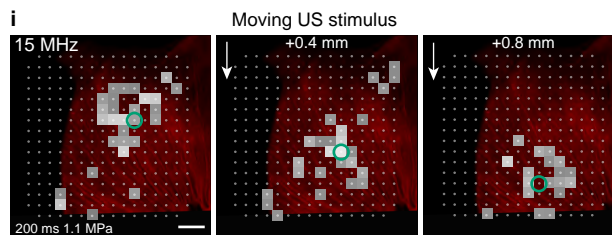
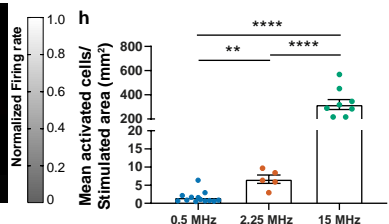
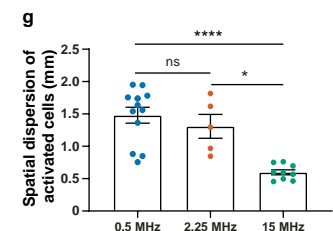
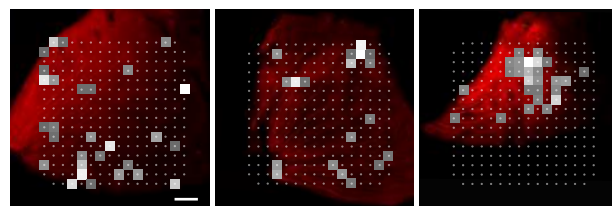
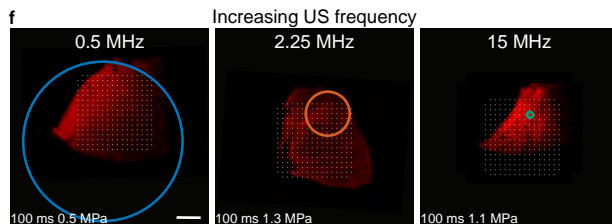
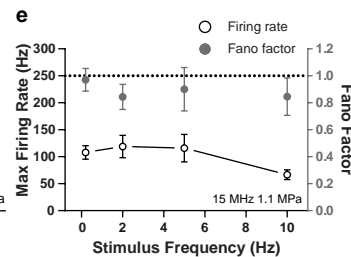
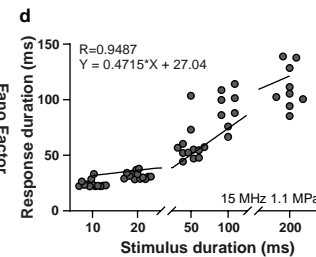
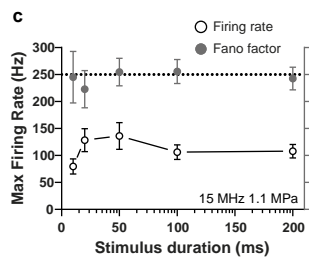
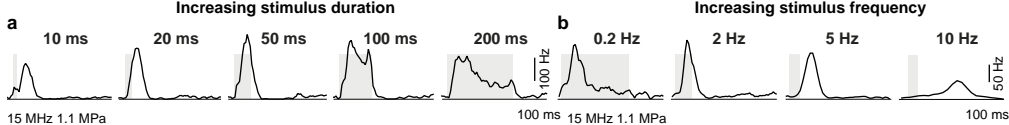
- 845 52. Jensen, J.A. & Svendsen, N.B. Calculation of pressure fields from arbitrarily shaped,
846 apodized, and excited ultrasound transducers. *IEEE Trans Ultrason Ferroelectr Freq*
847 *Control* **39**, 262-267 (1992).
- 848 53. Jensen, J.A. A Program for Simulating Ultrasound Systems. *Medical & Biological*
849 *Engineering & Computing* **34**, 351-353 (1996).
- 850 54. DATABASE., I.F. Available at: [https://itis.swiss/virtual-population/tissue-](https://itis.swiss/virtual-population/tissue-properties/database)
851 [properties/database](https://itis.swiss/virtual-population/tissue-properties/database). (Accessed: 17th August 2020).
- 852 55. McIntosh, R.L. & Anderson, V.A. A comprehensive tissue properties database
853 provided for the thermal assessment of a human at rest. *Biophysical Reviews and*
854 *Letters* **5**, 129–151 (2010).

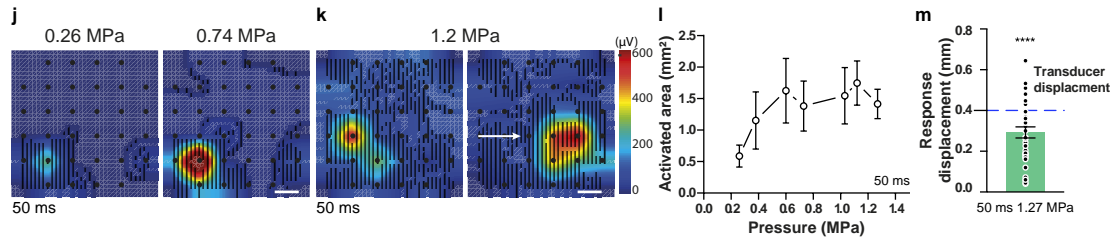
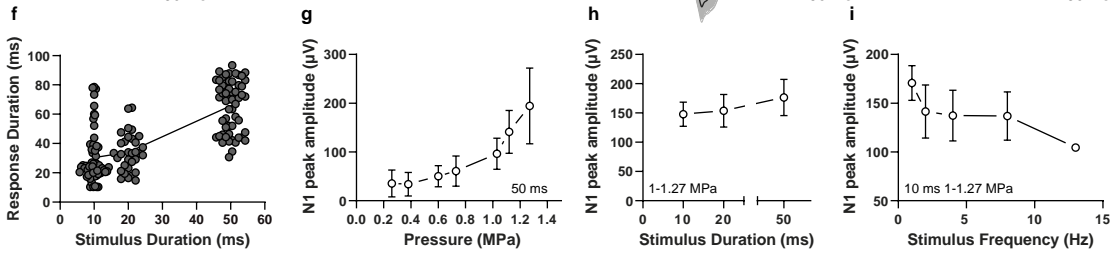
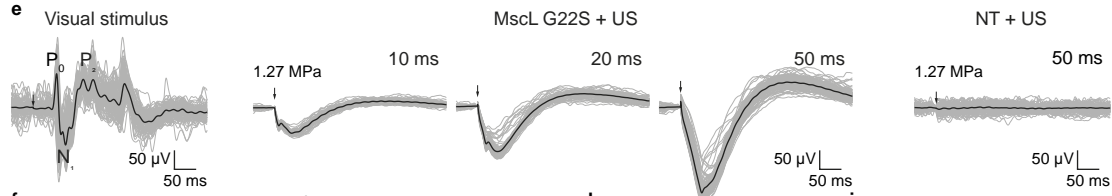
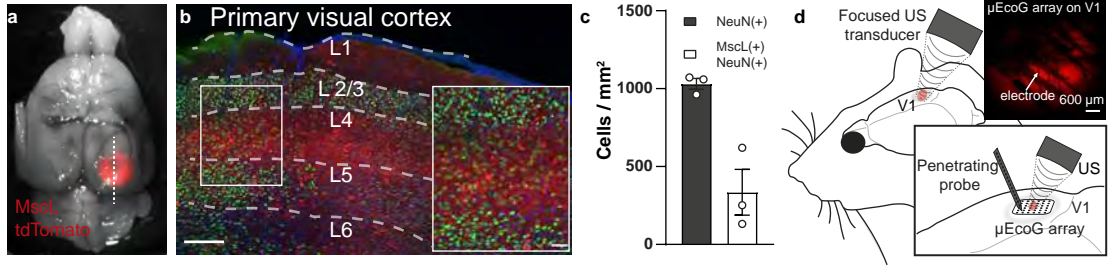
855

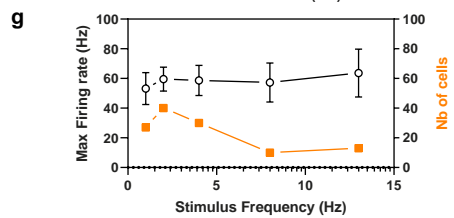
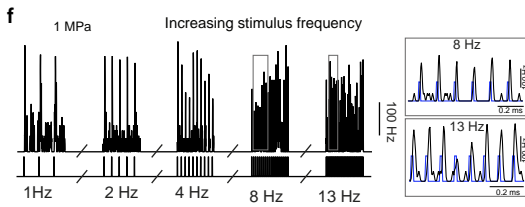
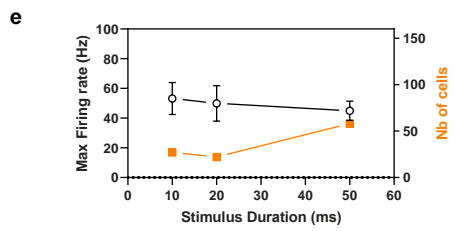
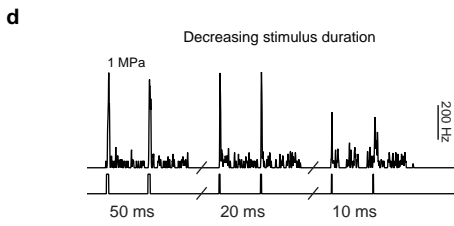
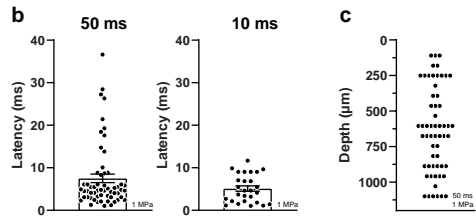
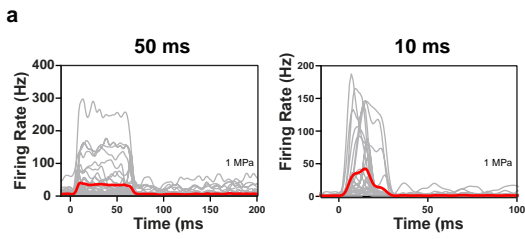
856

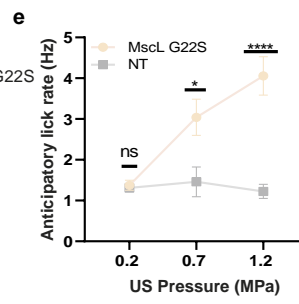
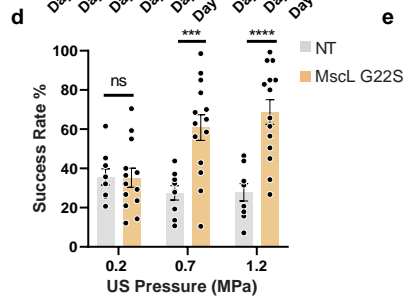
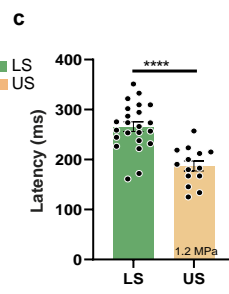
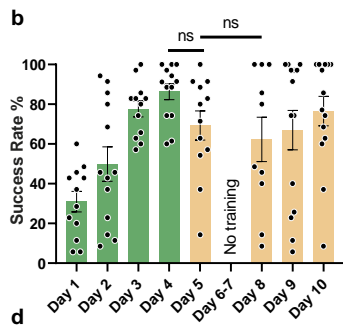
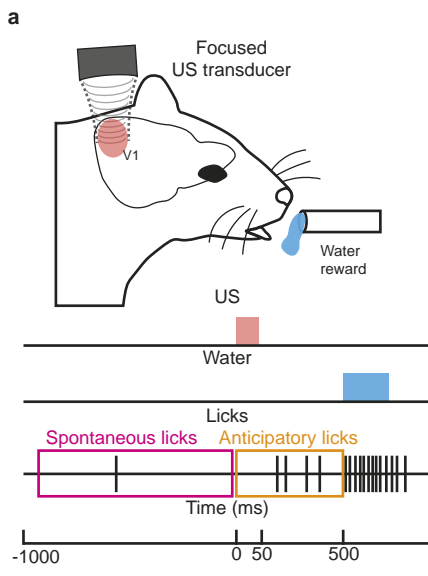












1 **Extended data figures:**

2

3 **Fig. E1 Retinal expression of MscL.** (a) Whole-mount retina expressing MscL WT (red) and labeled with
4 the RGC-specific anti-RBPMS antibody (green), with DAPI staining of the nucleus (white). Yellow boxes
5 represent the 8 zones selected for the counting of MscL- and RBPMS-positive cells. (b) Optical section
6 of a confocal stack showing MscL expression limited to the ganglion cell layer. The scale bars represent
7 1 mm in (a), 50 μm in (b). Similar results have been obtained for N=10 retinas (5 expressing MscL WT
8 and 5 expressing MscL G22s).

9

10
11 **Fig.E2 Retinal sonogenetic response characteristics for US stimuli of different frequencies.** (a) Mean
12 distribution of the different RGC cell types (ON, OFF, ON-OFF) among short (SL) and long latency (LL)
13 responses in retinas ($n=9$) expressing MscL (WT and G22s form) following a 15 MHz US stimulus (SD:
14 21.6, 28.0, 21.8 % for SL, 34.7, 19.4, 30.3 % for LL cells, for ON, ON-OFF and OFF cells respectively). (b)
15 Mean numbers of RGCs responding to a 15 MHz stimulus of increasing acoustic pressure for MscL WT
16 ($n=3$), MscL G22s ($n=5$) and NT ($n=4$) retinas (0.39 MPa: * $p=0.0163$; 0.54 MPa: ns $p=0.1480$, *
17 $p=0.0168$; 0.74 MPa: ns $p=0.1334$, * $p=0.0312$; 0.96 MPa: * $p=0.0462$, * $p=0.0279$; 1.15 MPa: ns
18 $p=0.1617$, * $p=0.0145$; 1.27 MPa: ns $p=0.1580$, * $p=0.0144$; unpaired two-tailed t test between MscL
19 WT and NT in gray and MscL-G22s and NT in blue). (c) Scatter plots and geometric means of RGC
20 latencies in response to a 15 MHz US stimulus for MscL ($n=300$ cells SD: 48.8), Blockers+MscL ($n=57$
21 cells, SD: 68.0), P23H+MscL ($n=97$ cells, SD: 37.5), and NT ($n=41$ cells, SD: 27.4) retinas (****, $p=7.3*10^{-8}$
22 for MscL and Blockers MscL vs NT and $p<.1*10^{-15}$ for P23H MscL vs NT, unpaired two-tailed t -test on
23 log-transformed values). (d) Cumulative frequency distribution of RGC latencies for MscL,
24 Blockers+MscL, P23H+MscL, and NT retinas. (e) Mean percentage of cells responding to US stimuli
25 (normalized against the maximum number of responsive cells in the experiment) of increasing acoustic
26 pressure for 0.5 MHz (ns $p=0.1661$; * $p=0.0292$; * $p=0.0260$; ns $p=0.8628$; ns $p=0.1316$; ns $p=0.7731$;
27 unpaired t test), 2.25 MHz (ns $p=0.1474$; ns $p=0.0522$; * $p=0.0140$; *** $p=0.0005$; **** $p<0.00002$; ns
28 $p=0.5000$; unpaired t test) and 15 MHz US (* $p=0.0382$; ** $p=0.0065$; * $p=0.0218$; ns $p=0.8628$; ns
29 $p=0.5859$; ns $p=0.4223$; unpaired t test) US. The lower x axis represents the corresponding acoustic
30 intensity (I_{spTa}). (f) Mean response latencies of SL cells for 0.5 and 2.25 MHz ($n=9$ and 8 retinas). Data
31 are presented as mean values +/- SEM.

32 **Fig. E3 Experimentally measured US pressure fields.** US pressure fds near the focus for 0.5, 2.25 and
33 15 MHz focused transducers, measured in water. Color-coded pressure maps in the *xy* and *xz* planes,
34 for 0.5, 2.25 and 15 MHz.

35 **Fig. E4 Simulated acoustic fields and temperature increases.** (a) Comparison between a water tank
36 measurement at the focus with a calibrated hydrophone (black) obtained with the 2.25 MHz
37 transducer and reaching -1.11 MPa peak negative pressure, and a simulated waveform at the focus
38 (blue) reaching the same negative pressure. The two waveforms match very well (0.42% error)
39 ensuring a good match between our simulation setup and physical parameters. (b) Power spectral
40 density of the measured (black) and simulated (blue) waveforms, showing that simulations can be used
41 to estimate the importance of non-linear propagation. A second harmonic 20 dB below the
42 fundamental indicates a factor of 100 in terms of energy, meaning that absorption can be calculated
43 in a linear approximation. (c-f) Thermal simulations are performed in a two-fold process corresponding
44 to a worst-case scenario (see methods): propagation in a water medium, and thermal absorption in a
45 brain-mimicking medium. (h) 3D temperature map at the end of a 200 ms stimulation (at 15 MHz and
46 1.27 MPa). (d) Temperature rise at the focus for a 15 MHz 200 ms stimulation with the 7 pressures
47 used in Fig. 1I (0.26, 0.39, 0.54, 0.74, 0.96, 1.15, 1.27 MPa). A zoom on the increasing curve reveals the
48 fluctuations due to the 1 kHz on-off cycles. (e) Temperature rise at the focus for a 15 MHz 50 ms
49 stimulation with the same 7 pressures. (f) Temperature rise at the focus for 15 MHz 10ms stimulations
50 (1 kHz modulation) at a repetition rate of 8 Hz and 13 Hz (used in figure 3o), for focus pressures of 0.96
51 MPa and 0.54 MPa.

52

53 **Fig. E5 In vivo response displacement to US stimulation.** (a) Relative displacement of the activation
54 center to the previous position following movement of the US transducer by 0.4 mm in the x and y
55 direction ($n=37$ positions on 6 animals). Data are presented as mean values \pm SEM.

56

57

58 **Fig. E6: MscL G22S expression with the US and light-associative training in mice.** (a) Confocal stack
59 projection of a sagittal brain slice expressing MscL G22s-tdTomato (red) and labeled with DAPI (blue).
60 Similar results have been obtained on N=3 animals. (b) Head-fixed and water-restricted mice were
61 trained for four days to respond to a full-field stimulation of one eye (200 and 50 ms) that preceded a
62 water reward. Mice responded by licking before (anticipation — successful trial) or after the delivery
63 of water (failure). The mean success rate increased progressively and mice learned the task (upon 50
64 ms and 200 ms light stimulation) after four days of training (ns $p=0.9387$, two-tailed unpaired t test,
65 Mean: 27.9, 45.4, 77.1, 88.8, SD: 17.4, 24.8, 23.6, 10.4% for 200ms, Mean: 30.7, 54.2, 75.9, 88.5, SD:
66 22.2, 31.0, 17.5, 12.8% for 50ms). (c) Mean rates of successful trials in non-transfected (NT) mice for 4
67 days of training with light stimulation (50 ms, LS green) and for 4 days of US stimulation (US orange)
68 (Between Day 4 LS and Day 5 US: 50 ms 1.2 MPa, ****, $p=0.0000047$, two-tailed unpaired t test.
69 Between Day 5 US and Day 8 US: 50 ms 1.2 MPa, ns, $p=0.1850$. Mean: 30.5, 60.3, 73.6, 91.7, 38.1, 23.5,
70 14.3, 34.0, SD: 28.2, 31.6, 22.1, 10.3, 18.5, 25.5, 21.1, 24.4 %). (d) Pearson correlation scatter plot for
71 time to first lick after either light (LS) or US stimulation. (e) Identification and exclusion of outlier
72 sessions (in red) based on the ROUT method, ($Q = 1\%$) for the session spontaneous lick rate measured
73 on a 1s time window prior to all trials of the session e $Q_1= 0.9$ Hz, Median = 1.7 Hz, $Q_3= 2.8$ Hz, Mean=
74 2.3 Hz, SD= 2.3 Hz. Data are presented as mean values +/- SEM.

